Symmetry-adapted order parameters and free energies for solids undergoing order-disorder phase transitions

Anirudh Raju Natarajan, John C. Thomas, Brian Puchala, and Anton Van der Ven

Phys. Rev. B **96**, 134204 — Published 23 October 2017

DOI: 10.1103/PhysRevB.96.134204

Symmetry adapted order parameters and free energies for solids undergoing order-disorder phase transitions

Anirudh Raju Natarajan,[1] John C. Thomas,[1] Brian Puchala,[2] and Anton Van der Ven[1,*]

[1] *Materials Department, University of California, Santa Barbara*

[2] *Department of Materials Science and Engineering, University of Michigan, Ann Arbor*

(Dated: August 16, 2017)

Accurate thermodynamic descriptions are a key ingredient to kinetic theories that describe the mesoscale evolution of a solid undergoing ordering or decomposition reactions. We introduce a general approach to identify order parameters for order-disorder reactions and to calculate first-principles free energy surfaces as a function of these order parameters. The symmetry of the disordered phase is used to formulate order parameters as linear combinations of sublattice compositions of a reference supercell. The order parameters can distinguish the disordered phase from the symmetrically equivalent variants of a particular ordered phase. A thermodynamic formalism is then developed to rigorously define a coarse grained free energy as a function of order parameters. Bias potentials are added to the potential energy to enable sampling of the unstable regions within the order parameter domain. Monte Carlo sampling in the biased ensemble is combined with free energy integration to calculate high-temperature free energies. We illustrate the approach by analyzing the free energies of order-disorder transitions on a two-dimensional triangular lattice and in the technologically important Ni-Al alloy.

I. INTRODUCTION

Order-disorder transformations in alloys have been the focus of research since the early 1900's. Since then, various methods to model and characterize these phenomena have been developed. A number of metallurgical alloys exploit ordering transformations to achieve a variety of desirable properties. For example, a dispersion of ordered-precipitates, coherently embedded within a matrix phase can lead to a dramatic strengthening of an alloy as it impedes dislocation glide. Precipitation hardening is commonly applied to nickel-based superalloys[1,2] to increase their creep resistance and to aluminum and magnesium alloys[3–6] to enhance their strength.

Order-disorder phenomena are not just limited to metallurgical alloys, but can also play an important role in functional materials. Ordering reactions have been used to develop superior thermoelectric materials with a low thermal conductivity through the formation of multiphasic microstructures[7–9]. The ability to control the degree of ordering on the surfaces of catalyst alloys has also been recognized as a lever with which to improve catalytic efficiencies[10–14]. However, ordering is not always desirable. The onset of cation ordering within the electrodes and electrolytes of electrochemical energy storage devices is often accompanied by a reduction in cation mobility[15–17]. Strategies are, therefore, actively sought with which to suppress ordering among mobile species[18].

The phase field method can model the temporal and spatial evolution of a solid undergoing order-disorder transformations at the mesoscale[19–24]. The beginnings of this method can be traced back to the work of Cahn, Hilliard and Allen[19,20]. A key step in formulating a phase field model for a particular order-disorder transformation is the identification of suitable order parameters that can distinguish the ordered phase from the disordered phase. Other essential ingredients include homogeneous free energies (as a function of temperature, composition and order parameters), gradient energy coefficients and atomic mobilities. Several approaches have been developed to link these quantities directly to the electronic structure of the alloy using first-principles statistical mechanics approaches[25–40]. However, the formulation of suitable order parameters for arbitrarily complex order-disorder transformations and the calculation of free energies as a function of those order parameters has remained elusive.

Here, we introduce a general approach to identify order parameters for any order-disorder transformation within a multi-component crystalline solid (meant to broadly include metallic alloys, oxides, semiconductors, surfaces, etc.). We also develop an approach to calculate first-principles free energies as a function of those order parameters, both in regions where the free energy is convex and where it is concave. We apply this methodology to study the thermodynamics of ordering predicted by the triangular lattice-model Hamiltonian with nearest and next-nearest neighbor interactions and to shed light on ordering phenomena observed in the technologically important Ni-Al alloy.

II. GENERATING ORDER PARAMETERS

The formation of an ordered phase from a disordered solid solution leads to a reduction in symmetry. The high symmetry disordered phase can transform to one of several symmetrically equivalent variants of the ordered phase.

Order parameters that describe this lowering of symmetry must satisfy several criteria. The order parameters must be able to distinguish between the disordered phase and the ordered phase of interest. Furthermore, they must be able to distinguish between the symmetrically equivalent variants of a particular ordered phase. The definition of the order parameters must prescribe a mapping of any arbitrary configuration of atoms within the crystal onto a point in the space defined by the order parameters (Figure 1). The function that performs this mapping may map several configurations onto the same point in order parameter space. Such a many-to-one mapping is desired as the aim is to minimize the number of descriptors needed to characterize the symmetry breaking of the ordering process. The following sections describe an approach to formulate order parameters for any order-disorder reaction in a crystalline solid.

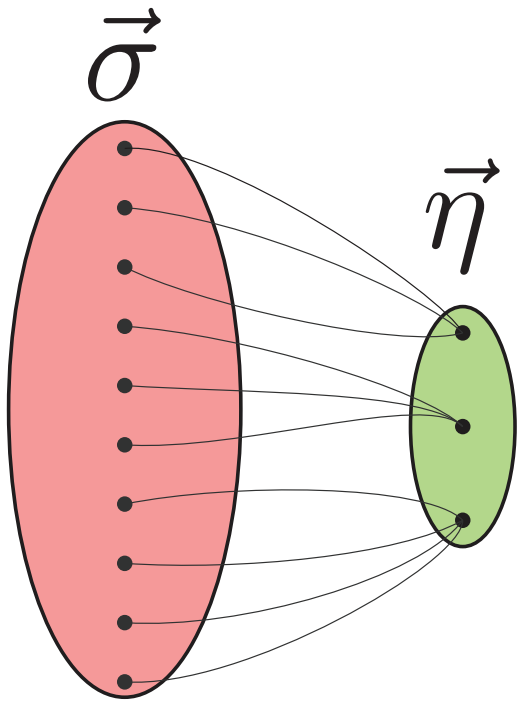

FIG. 1. Schematic picture showing the function mapping an arbitrary configuration ($\vec{\sigma}$) to a value of the order parameters ($\vec{\eta}$)

A. Order parameters from sublattice compositions

Conventionally, the order parameters for simple orderings such as B2, $D0_{19}$ and $L1_2$ are written as linear combinations of sublattice compositions. We illustrate this for a binary substitutional alloy consisting of A and B atoms. An ordered phase is then a particular arrangement of A and B atoms on the sites of a parent crystal structure that repeats itself periodically throughout the whole crystal. The periodicity of the ordering can be described with translation vectors that define a supercell of the primitive cell of the parent crystal structure. The supercell consists of s sublattices. It is convenient to associate a composition variable x_p with each sublattice $p = 1, ..., s$ of a reference supercell. For a crystal containing M supercells, the sublattice compositions can be defined as

$$x_p = \frac{N_p^{\mathrm{B}}}{M}. \tag{1}$$

where N_p^{B} is the number of B atoms on all sites related to sublattice p by the translational symmetry of the supercell. We will denote the collection of sublattice compositions as a vector containing s entries, i.e. $\vec{x} = [x_1, x_2, \cdots, x_s]^T$.

As an example, consider the CsCl type B2 ordering on the BCC parent crystal structure shown in Figure 2. The smallest supercell of B2 is the conventional cubic unit cell of BCC. Figure 2 labels the two sublattice sites within this supercell. The two sublattice compositions, x_1 and x_2, are sufficient to characterize both the disordered phase (i.e. $x_1 = x_2$) and the two translational variants of B2 (i.e. $x_1 = 1$ and $x_2 = 0$ for one translational variant and $x_1 = 0$

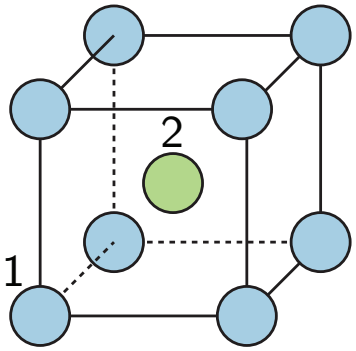

FIG. 2. Conventional cell of BCC, showing 2 sublattices

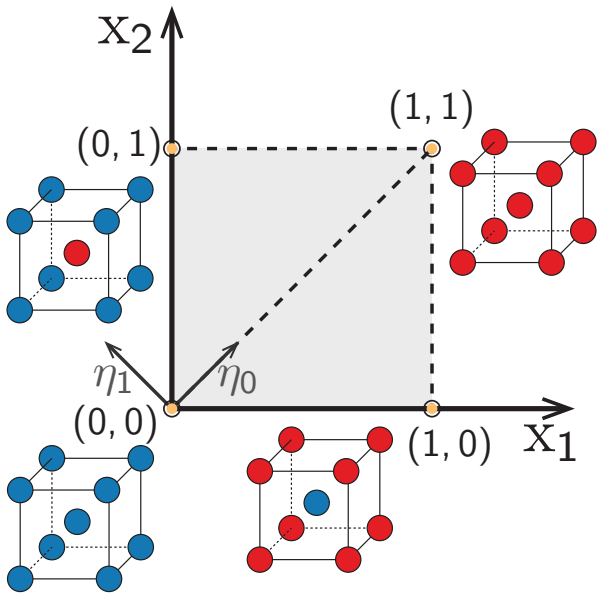

FIG. 3. Schematic of the space spanned by the sublattice compositions of fig. 2. The figure shows the four orderings commensurate with this supercell, as well as the reorientation of the space defined by eqs. (2) and (3)

and $x_2 = 1$ for the other). However, the same information can be more conveniently represented with the following linear combinations of the sublattice compositions:

$$\eta_0 = \frac{x_1 + x_2}{2} \tag{2}$$

$$\eta_1 = \frac{x_1 - x_2}{2} \tag{3}$$

The order parameters, η_0 and η_1, span the same space as the sublattice compositions, albeit rotated by 45° (Figure 3). The first order parameter, η_0, corresponds to the overall composition of the alloy and is independent of the degree of long-range order. The second order parameter, η_1, in contrast, measures the degree of long-range B2 order and is exactly zero in the absence of any long-range order. Transforming from the $x_1 - x_2$ coordinate system to the $\eta_0 - \eta_1$ coordinate system corresponds to a reorientation of the space such that the disordered solid solution falls on the line defined by $\eta_1 = 0$. Furthermore, the sign of η_1 distinguishes the two symmetrically equivalent translational variants of B2 as they occur at different points in this space: at $\eta_0 = \frac{1}{2}$, one translation variant of perfectly ordered B2 has $\eta_1 = \frac{1}{2}$ while the other translational variant has $\eta_1 = -\frac{1}{2}$. The order parameters of Equations (2) and (3) qualitatively split the sublattice composition space into two. Though the exact same information is represented by

both coordinates systems, the order parameters, η_0 and η_1, are more insightful since one of them (i.e. η_1) naturally captures the symmetry breaking that occurs upon ordering.

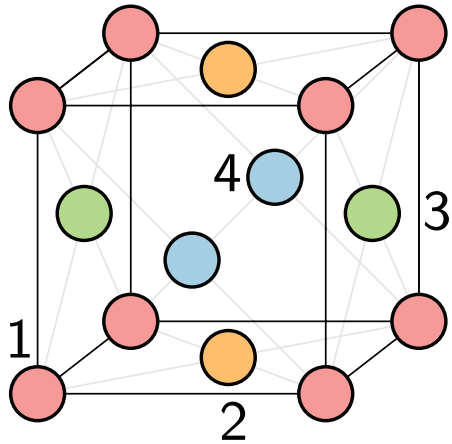

FIG. 4. Sublattices in the conventional FCC crystal structure, labelled 1-4.

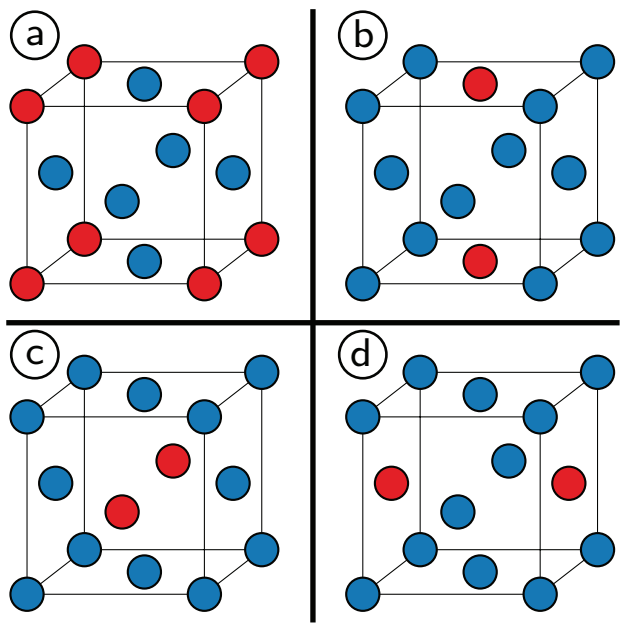

FIG. 5. Crystal structure of the $L1_2$ (A_3B) ordering on the FCC crystal structure. This ordering has four symmetrically equivalent translational variants.

Sublattice compositions can also be used to describe $L1_2$ ordering on the FCC parent crystal. The periodicity of the $L1_2$ ordering is that of the conventional cubic FCC unit cell containing four sublattices (fig. 4). There are four symmetrically equivalent translational variants of $L1_2$ (fig. 5). Order parameters can be defined as linear combinations of the sublattice compositions x_1, x_2, x_3 and x_4 according to[41]:

$$\eta_0 = \frac{x_1 + x_2 + x_3 + x_4}{4} \tag{4}$$

$$\eta_1 = \frac{x_1 + x_2 - x_3 - x_4}{4} \tag{5}$$

$$\eta_2 = \frac{x_1 - x_2 - x_3 + x_4}{4} \tag{6}$$

$$\eta_3 = \frac{x_1 - x_2 + x_3 - x_4}{4} \tag{7}$$

Similar to B2, η_0 corresponds to the overall composition of the alloy, while the remaining order parameters, η_1, η_2 and η_3, describe the symmetry breaking accompanying $L1_2$ type ordering. The linear combinations separate the four-dimensional sublattice composition space into two qualitatively distinct subspaces: a one-dimensional subspace corresponding to the global composition and a three-dimensional subspace that tracks the degree of long range order similar to $L1_2$. In the disordered state, the order parameters η_1,η_2 and η_3 all equal zero. Non-zero values of η_1, η_2 and η_3 correspond to configurations with partial long-range order similar to $L1_2$. At a composition of $\eta_0 = 0.25$, all allowed configurations map onto points inside a tetrahedron in η_1,η_2 and η_3 space as illustrated in fig. 6. The vertices of the tetrahedron correspond to the four perfectly ordered translational variants of $L1_2$. The η_1,η_2 and η_3 coordinates are therefore suitable order parameters to distinguish the four translational variants of $L1_2$ from each other and from the disordered phase.

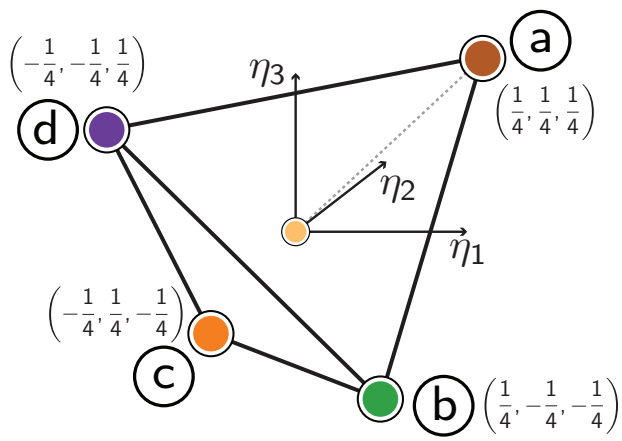

FIG. 6. Schematic of the domain of η_1, η_2, and η_3 values spanned by real configurations at a composition of η_0=0.25. Perfect $L1_2$ type orderings are formed at the corners of the tetrahedron. The disordered phase with the same composition is mapped on to the origin of this domain.

The two examples illustrate that particular linear combinations of sublattice compositions of a reference supercell can generate a set of order parameters that can be partitioned into qualitatively distinct subspaces, each describing different aspects of the ordered and disordered phases. The B2 and $L1_2$ order parameters can be thought of as coordinates in a space that has been rotated relative to the s sublattice composition axes. The axes of the order parameter space are aligned with high symmetry directions of the sublattice composition space. The re-orientation allows a natural partitioning of the space into symmetrically distinct sub-spaces that describe different types of symmetry breaking. Not all subspaces are needed to distinguish between the different translational variants of the ordered phase and the disordered phase, thus allowing a reduction in the number of variables needed to describe the phase transition.

In general, when seeking to identify order parameters for a particular ordering, it is necessary to determine a suitable coordinate transform that converts the sublattice compositions, $\vec{x}$, to the desired order parameters, $\vec{\eta}$, according to

$$\boldsymbol{Q}\vec{x} = \vec{\eta}, \tag{8}$$

where $\boldsymbol{Q}$ is a $s \times s$ rotation matrix that satisfies $\boldsymbol{Q}^T\boldsymbol{Q} = \boldsymbol{I}$ (with $\boldsymbol{I}$ the identity matrix). As the B2 and $L1_2$ examples illustrate, the choice of $\boldsymbol{Q}$ is motivated by the effect of operations in the space group of the parent crystal on the sublattice compositions. The application of a particular symmetry operation of the parent crystal is equivalent to permuting the sublattices in the reference supercell. This can be represented mathematically as a matrix multiplication

$$\vec{x}' = \boldsymbol{A}^{(i)}\vec{x} \tag{9}$$

where $\vec{x}'$ and $\vec{x}$ are sublattice concentrations corresponding to two symmetrically equivalent orderings related to each other by a symmetry operation i of the parent crystal and where the matrix $\boldsymbol{A}^{(i)}$ represents the effect of that symmetry operation on the sublattice compositions. The symmetry representations that act on the sublattice compositions

according to Eq. 9 are all permutation matrices. For instance, the representation of any symmetry operation of the BCC crystal that acts on the two sublattice compositions of the B2 supercell (Figure 2) takes one of two forms:

$$\boldsymbol{A}^{(1)} = \begin{pmatrix} 1 & 0 \\ 0 & 1 \end{pmatrix} \quad \boldsymbol{A}^{(2)} = \begin{pmatrix} 0 & 1 \\ 1 & 0 \end{pmatrix} \tag{10}$$

The matrix $\boldsymbol{A}^{(1)}$ is the symmetry representation of all BCC space group symmetry operations that leave the sublattice sites in place, while $\boldsymbol{A}^{(2)}$ is the symmetry representation for the space group operations that permute the two sublattice sites. The factor group of the reference supercell of B2 contains 96 operations, 48 of which are represented by $\boldsymbol{A}^{(1)}$ and the rest by $\boldsymbol{A}^{(2)}$.

Group theory tells us that the rotation matrix, $\boldsymbol{Q}$, will simultaneously block-diagonalize all the symmetry matrices $\boldsymbol{A}^{(i)}$. The matrix representations, $\tilde{\boldsymbol{A}}^{(i)}$, acting on $\vec{\eta}$ for each space group symmetry operation i of the parent crystal are related to the matrix representations $\boldsymbol{A}^{(i)}$ that act on $\vec{x}$ according to:

$$\tilde{\boldsymbol{A}}^{(i)} = \boldsymbol{Q}\boldsymbol{A}^{(i)}\boldsymbol{Q}^{-1} = \boldsymbol{Q}\boldsymbol{A}^{(i)}\boldsymbol{Q}^{T}, \tag{11}$$

This relation follows upon substitution of Equation (8) into Equation (9). Therefore, in order to identify *symmetry adapted* order parameters for a particular order-disorder transition, it is simply necessary to find a rotation matrix $\boldsymbol{Q}$ such that every distinct matrix $\tilde{\boldsymbol{A}}^{(i)}$ given by Eq. 11, has the same block diagonal structure. Simultaneous block diagonalization of the set of symmetry matrices $\boldsymbol{A}^{(i)}$ to yield $\tilde{\boldsymbol{A}}^{(i)}$ and $\boldsymbol{Q}$ can be performed using an algorithm described by Thomas and Van der Ven[42].

Once all symmetry representations, $\tilde{\boldsymbol{A}}^{(i)}$, are in the same block diagonal form, the space of order parameters is split into a number of subspaces with lower dimensionality than s. Each sub-space has as many dimensions as the size of the blocks in its symmetry representation. Block-diagonal symmetry operations can only transform vectors in a particular sub-space (i.e., block) into other vectors in the same sub-space. As such, these subspaces are thus invariant under the application of symmetry. Group theory shows that if a block-diagonal symmetry representation cannot be partitioned into smaller subspaces by subsequent block-diagonalization, then the blocks correspond to *irreducible representations* of the group, and the basis vectors that span their corresponding subspaces transform according to these irreducible representations. There is always a one-dimensional subspace corresponding to the composition of the alloy, which is invariant to symmetry.

B. Accounting for orientational variants

The general approach outlined in the previous section will generate a complete set of symmetry adapted order parameters that describe the symmetry breaking accompanying an ordering transformation within a specific reference supercell. Unlike $L1_2$ and B2, most ordered phases have supercells that are not invariant to the point group of the parent crystal structure. Symmetrically equivalent variants may have supercells that have different orientations, leading to some ambiguity in indentifying appropriate sublattice concentrations.

As an example, consider the (2×1) row ordering on the triangular lattice shown in fig. 7. Due to the three-fold symmetry of the triangular lattice, there are three symmetrically equivalent orientations of the (2×1) row ordering. As shown in fig. 7, the smallest supercells associated with the three orientations of row orderings are not the same.

Formally, the relationship between a supercell ($\boldsymbol{S}$) and a primitive lattice ($\boldsymbol{P}$) can be written as a matrix multiplication:

$$\boldsymbol{S} = \boldsymbol{P}\boldsymbol{T} \tag{12}$$

where $\boldsymbol{P} = [\vec{a}, \vec{b}, \vec{c}]$ and $\boldsymbol{S} = [\vec{A}, \vec{B}, \vec{C}]$ are matrices containing the lattice vectors of the primitive and supercells respectively and the transformation matrix $\boldsymbol{T}$ is a full-rank integer matrix with the same dimensions as $\boldsymbol{P}$ and $\boldsymbol{S}$. For two-dimensional lattices, the primitive and supercell matrices are of dimensions 2×2, while for 3-dimensional lattices they are 3×3. The supercell transformation matrices for the three orientational variants of the (2×1) row ordering on the triangular lattice are:

$$\boldsymbol{T}^{(1)} = \begin{pmatrix} 1 & -1 \\ 0 & 2 \end{pmatrix} \quad \boldsymbol{T}^{(2)} = \begin{pmatrix} 0 & -2 \\ 1 & 1 \end{pmatrix} \quad \boldsymbol{T}^{(3)} = \begin{pmatrix} 1 & 1 \\ -1 & 1 \end{pmatrix} \tag{13}$$

We refer to equivalent variants having different primitive supercells as *orientational* variants. But as with the simpler orderings such as B2 and $L1_2$, there are usually also several *translational* variants per orientational supercell. The (2×1) row ordering has two translational variants for each orientational supercell since the smallest supercell

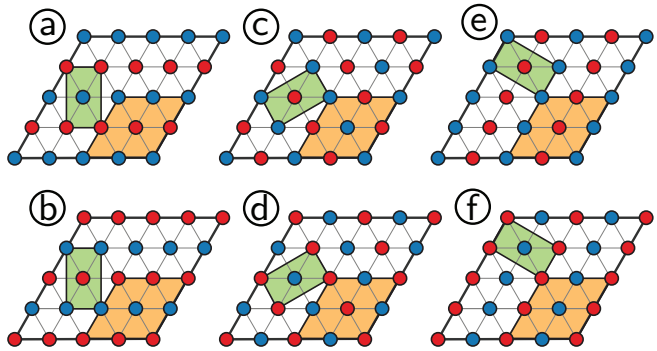

FIG. 7. Variants of the (2×1) ordering on the triangular lattice. The primitive cell required to describe each ordering is highlighted in blue, while the decoration of each variant in the *mutually commensurate* cell is highlighted in orange.

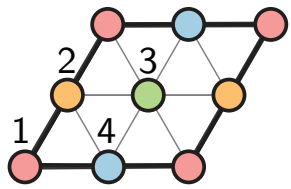

FIG. 8. Reference cell that can accommodate all the translational and orientational variants of the 2×1 ordering on the triangular lattice. The cell contains four sublattices that are labeled as shown in the figure.

that describes this ordering contains two lattice sites of the underlying triangular lattice. This results in a total of six symmetrically equivalent variants of the row ordering on the triangular lattice.

In order to identify symmetry adapted order parameters for more complicated orderings that have both orientational and translational variants, it is necessary to work with a supercell and accompanying sublattice concentrations that can describe all variants simultaneously. For example, the smallest supercell that is commensurate with the three orientational supercells of the (2×1) row ordering (Eq. 13) has the transformation matrix:

$$\mathcal{T} = \begin{pmatrix} 2 & 0 \\ 0 & 2 \end{pmatrix}. \tag{14}$$

This *mutually commensurate* supercell is illustrated in fig. 8 and is clearly a supercell of all three primitive orientational supercells of the (2×1) row orderings. The sublattice concentrations of the *mutually commensurate* supercell serve as an appropriate basis with which to construct symmetry adapted order parameters that describe all orientational and translational variants of the row ordering as well as the disordered phase.

Once the mutually commensurate supercell has been established for a particular ordering we can apply the approach described in the previous section to identify the transformation matrix linking the sublattice concentrations within this supercell to the symmetry adapted order parameters. For the row ordering using the mutually commensurate supercell of Eq. 14 to specify sublattice concentrations, this transformation matrix takes the form

$$\boldsymbol{Q} = \frac{1}{4} \begin{pmatrix} 1 & 1 & 1 & 1 \\ 1 & 1 & -1 & -1 \\ 1 & -1 & 1 & -1 \\ 1 & -1 & -1 & 1 \end{pmatrix} \tag{15}$$

The rows of the transformation matrix, $\boldsymbol{Q}$, correspond to the linear combinations of the sublattice compositions that yield the order parameters.

The symmetry matrices that act on the order parameter space for the row ordering are block diagonal with dimensionalities of 1 and 3. This means that the first order parameter does not mix with the other three variables upon application of symmetry of the parent crystal. The one-dimensional space containing only the first order parameter (or row) corresponds to the average value of the sublattice compositions and is therefore equal to the global composition. The next three rows correspond to three order parameters that distinguish between the ordered variants and the disordered state. At a composition of 0.5, the values of the order parameters η_1, η_2 and η_3 for the variants of the

row ordering reside at the vertices of an octahedron (fig. 9). Each order parameter describes a particular orientational variant while its sign describes a translational variant. Points with perfect ordering have coordinates such as $\left(\frac{1}{2}, 0, 0\right)$. The origin of this space (i.e. $(0, 0, 0)$) corresponds to the disordered phase.

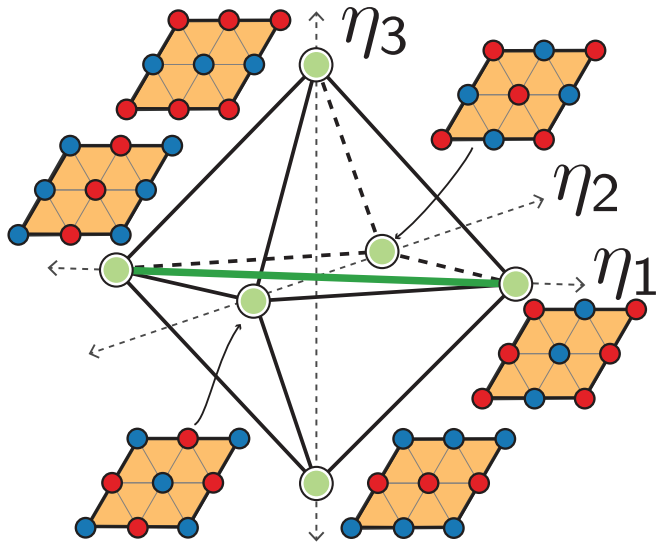

FIG. 9. Schematic of the η_1, η_2, η_3 domain for the triangular lattice at a composition (η_0) of 0.5. Each row ordering is formed at the corners of the octahedron. The disordered phase is mapped on to the origin.

C. A summary of the algorithm for a general ordering

In this section we summarize and generalize the approach to determine symmetry adapted order parameters for any order-disorder transformation on a multi-component crystalline solid. The first step is to determine the mutually commensurate supercell that can accommodate all orientational variants of the ordered phase. Applying the point group of the undecorated parent crystal structure to the supercell of a "seed" ordering will generate a set of transformation matrices, $\mathbb{T}$, containing all orientational variants:

$$\mathbb{T} = \{\boldsymbol{T}^{(1)}, \boldsymbol{T}^{(2)}, \cdots\} \tag{16}$$

Each $\boldsymbol{T}^{(i)}$ is a transformation matrix for a particular orientational variant relative to the primitive cell. In the case of the triangular lattice, the set of transformation matrices are given by Equation (13). The transformation matrix ($\mathcal{T}$) of the mutually commensurate supercell must be a solution to the following equation:

$$\boldsymbol{P}\mathcal{T} = (\boldsymbol{P}\boldsymbol{T}^{(i)})\boldsymbol{V}^{(i)}, \forall \boldsymbol{T}^{(i)} \in \mathbb{T} \tag{17}$$

where $\boldsymbol{V}^{(i)}$ and $\mathcal{T}$ are integer matrices. The left hand side of Equation (17) denotes a supercell that is related to the primitive cell ($\boldsymbol{P}$) through the integer transformation matrix $\mathcal{T}$. The right hand side of the equation denotes the relationship of the same cell to each of the orientational variants ($\boldsymbol{P}\boldsymbol{T}^{(i)}$) through another integer transformation matrix $\boldsymbol{V}^{(i)}$. Equation (17) is a constraint that is satisfied only by a supercell of the primitive cell that is also a supercell of *all* the orientational variants in $\mathbb{T}$. A solution for $\mathcal{T}$ can be found by counting over all symmetrically distinct supercells of a crystal and checking if Equation (17) is satisfied. Algorithms to generate the symmetrically unique cells in increasing order of volume are described and implemented elsewhere[43,44]. Although there are many possible solutions for $\mathcal{T}$, we choose the one with the smallest volume. While this choice is not necessary, it reduces the number of sublattice sites that need to be explicitly considered. An efficient algorithm for the generation of the mutually commensurate supercell is described in appendix A.

The mutually commensurate supercell is used as the reference supercell to define a set of sublattice compositions. A rotation of the space spanned by the sublattice compositions, into a space that block-diagonalizes their symmetry representations should next be determined using the algorithm described by Thomas and Van der Ven[42]. The corresponding rotation matrix $\boldsymbol{Q}$ specifies, via eqs. (8) and (11), the s independent order parameters and their associated

block-diagonal symmetry representations. The order parameter subspaces identified via the block-diagonalization of the symmetry representations each correspond to particular classes of symmetry breaking.

Taken together, the generated order parameters can distinguish between all the 2^s possible orderings of a binary alloy within the reference supercell. Usually, we are interested in describing only a small subset of these orderings. Not all s order parameters are always needed to distinguish among a small subset of the 2^s possible orderings. Calculating the order parameters across all the symmetrically equivalent variants of an ordering shows that some of the order parameter subspaces have zero or identical values in all variants. Because such order parameters do not aid in distinguishing between orderings of interest, they can be discarded for the purpose of many thermodynamic analyses.

Mathematically, we can identify the minimal subset of the full s-dimensional order parameter space that are needed to describe a particular ordered phase as follows. The sublattice compositions across the m symmetrically equivalent variants ($\vec{x}^{(i)}$) of a particular ordering can be collected in a matrix $\boldsymbol{V}$ with the columns containing the sublattice occupancies for each variant:

$$\boldsymbol{V} = \left[\vec{x}^{(1)} \;\; \vec{x}^{(2)} \;\; \cdots \;\; \vec{x}^{(m)}\right] \tag{18}$$

The value of the order parameter for each of these variants can be calculated from Equation (8) as $\boldsymbol{\xi} = \boldsymbol{QV}$. Here, $\boldsymbol{\xi}$ is an $s \times m$ matrix, where each column is the value of the order parameters for a particular variant. A particular row, i of $\boldsymbol{\xi}$ corresponds to the values of order parameter η_i in each variant. If each element in a row i of $\boldsymbol{\xi}$ is identical across all variants (columns), then order parameter η_i does not provide any information with which to distinguish the different variants. Order parameter η_i is therefore superfluous and need not be considered to track the degree of long-range order. These order parameters correspond to directions in $\vec{x}$-space that are orthogonal to the space spanned by the orderings.

The above steps can be further generalized to generate order parameters if we are interested in distinguishing among several different types of ordering that are not all symmetrically equivalent. This collection of orderings may occur at different compositions and exhibit different super lattice periodicities. The set of transformation matrices ($\mathbb{T}$) in Equation (16) must be extended to include the orientational variants for all the orderings. The solution to Equation (17) is to be calculated across the larger set of transformation matrices. The larger reference supercell will then accommodate the orientational and translational variants of *all* orderings. The order parameters calculated in this reference supercell, via block-diagonalization of its factor group, can then be used to discern the minimal set of variables required to describe all the orderings of interest.

III. THERMODYNAMIC FRAMEWORK

Having outlined a general approach to generate order parameters for any order-disorder transformation in a crystal, we next describe a thermodynamic framework with which to calculate coarse-grained free energy as a function of these order parameters.

A. Legendre transforms, sublattice chemical potentials and the free energy

In order to construct a free energy description that explicitly depends on order parameters, we introduce sublattice chemical potentials. As with chemical potentials that are conjugate to the number of atoms of a particular species, it is possible to define a sublattice chemical potential that is conjugate to the number of atoms on each sublattice. The differential form of the Gibbs free energy of a (large) crystal when controlling the temperature, T, and the number of atoms on each sublattice can then be written as:

$$dG = -SdT + \sum_{i=1}^{s}\sum_{j=1}^{2} \mu_i^j dN_i^j \tag{19}$$

where G is the Gibbs free energy, S is the entropy, μ_i^j is the chemical potential of component j on sublattice i and N_i^j is the number of atoms of the jth component on the ith sublattice. (We assume a constant pressure and to be consistent with conventional first-principles total energy calculations set it equal to zero). The differential form of G in Eq. 19 indicates that the sublattice chemical potential is a partial derivative of the free energy according to

$$\mu_i^j = \left(\frac{\partial G}{\partial N_i^j}\right)_{T,p,N_{p\neq i}^{q\neq j}} \tag{20}$$

In a binary crystal having a fixed number of unit cells of the reference crystal, it is possible to rewrite Eq. 19 as

$$\begin{aligned} dG &= -SdT + M\sum_{i=1}^{s}(\mu_i^{\mathrm{B}} - \mu_i^{\mathrm{A}})dx_i \\ &= -SdT + M\vec{\mu}^T d\vec{x} \end{aligned} \tag{21}$$

where

$$\vec{\mu} = \vec{\mu}^{\mathrm{B}} - \vec{\mu}^{\mathrm{A}} \tag{22}$$

Here, $\vec{\mu}^{\mathrm{A}}$ and $\vec{\mu}^{\mathrm{B}}$ are vectors of dimension $s \times 1$ that contain the chemical potentials of A and B on each of the s sublattices.

It is convenient to work within the semi-grand canonical ensemble (SGC) to calculate coarse-grained free energies using Monte-Carlo and free energy integration techniques. In this ensemble, the controlled thermodynamic variables are the chemical potentials, $\vec{\mu}$, and the temperture with the total number of sites of the crystal held constant:

$$\Phi = G - M\vec{x}^T\vec{\mu} \tag{23}$$

M in this expression corresponds to the number of reference supercells that can tile the crystal. The differential form of the semi-grand canonical free energy takes the form

$$d\Phi = -SdT - M\vec{x}^T d\vec{\mu} \tag{24}$$

Inserting Equation (8), which relates the sublattice compositions, $\vec{x}$, to the order parameter, $\vec{\eta}$, in Equation (24), the differential form of the semi-grand canonical form becomes:

$$d\Phi = -SdT - M\vec{\eta}^T d\vec{\lambda} \tag{25}$$

where $\vec{\lambda}$ is defined as:

$$\vec{\lambda} = \boldsymbol{Q}\vec{\mu} \tag{26}$$

Just as the sublattice chemical potentials, $\vec{\mu}$, are conjugate to the sublattice compositions, the elements of $\vec{\lambda}$ are conjugate to the order parameters $\vec{\eta}$.

B. Coarse-grained free energies from first principles

Any ordering of A and B atoms in a crystal can be represented as a vector $\vec{\sigma}$, in which every element, σ_i contains an integer (-1 or $+1$) corresponding to the occupant (A or B) of site i. The free energy $G(x,T)$ as a function of the composition, x, of B species and temperature, T, can be expressed in terms of the partition function from statistical mechanics according to:

$$G(x,T) = -k_B T \ln Z(x,T) \tag{27}$$

with the partition function, Z, given by:

$$Z(x,T) = \sum_{\vec{\sigma}} \exp\left(-\frac{E(\vec{\sigma})}{k_B T}\right) \tag{28}$$

Here, $E(\vec{\sigma})$ is the formation energy of configuration $\vec{\sigma}$ and k_B is Boltzmann's constant. The sum is taken over all configurations, $\vec{\sigma}$, of the alloy having a composition x. Here we consider only configurational degrees of freedom, but other excitations (e.g. vibrational and electronic) can be incorporated in a straightforward manner as described by Ceder[30]. There are various methods to approximate $E(\vec{\sigma})$ in eq. (28). A common approach is to rely on a cluster expansion Hamiltonian parameterized with *ab-initio* density functional theory calculations[25,26].

The partition function, eq. (28), can be coarse grained to a sum over order parameters $\vec{\eta}$ for a particular ordered phase according to

$$Z(x,T) = \sum_{\vec{\eta}\in\Gamma_x} \exp\left(-\frac{G(\vec{\eta},T)}{k_B T}\right) \tag{29}$$

provided a coarse grained free energy is introduced that is defined as

$$G(\vec{\eta},T) = -k_B T \ln\left(\sum_{\vec{\sigma}} \exp\left(-\frac{E(\vec{\sigma})}{k_B T}\right)\delta\left(\vec{\eta}(\vec{\sigma})-\vec{\eta}\right)\right) \tag{30}$$

The Kronecker delta function, δ, is included to ensure that only configurations that map onto $\vec{\eta}$ according to the mapping function $\vec{\eta}(\vec{\sigma})$ contribute to the sum. The sum in eq. (29) extends over all values of $\vec{\eta}$ belonging to a domain Γ_x consistent with the composition x.

The above coarse graining scheme yields a free energy that is an explicit function of the order parameters $\vec{\eta}$. In most experimental situations it will not be possible to control the order parameters directly. Instead, the order parameters are internal degrees of freedom that adopt particular values once the solid has reached its equilibrium state. Away from critical phenomena, where the saddle-point approximation can be invoked[45], the solid in equilibrium will exhibit values of the order parameters $\vec{\eta}$ that minimize the coarse grained free energy $G\left(\vec{\eta},T\right)$.

From a practical point of view, it is more convenient to work within the semi-grand canonical ensemble for which Equation (24) is the characteristic potential. The partition function within this ensemble can be written as:

$$\Theta = \sum_{\vec{\sigma}} \exp\left(-\frac{E(\vec{\sigma}) - M\vec{\eta}^T\vec{\lambda}}{k_B T}\right) \tag{31}$$

where the sum now extends over all configurations and where the elements of $\vec{\lambda}$, conjugate to the order parameters $\vec{\eta}$, are linear combinations of the sublattice chemical potentials according to Eq. 26. This ensemble is more amenable for Monte-Carlo simulations as they can be performed by controlling the values of $\vec{\lambda}$ without the need to restrict the types of configurations that are sampled. Ensemble averages of thermodynamic quantities, including $\vec{\eta}$ and the average energy $\bar{E}$, etc. can then be calculated as a function of T and $\vec{\lambda}$. Relationships between ensemble averages and T and $\vec{\lambda}$ can then be integrated to yield free energies as is commonly done for alloys[35,46,47].

Conventional free energy integration approaches can only be used to calculate the stable parts of the free energy surface[35,46,47]. However, to serve as meaningful input to phase field model studies it is also of interest to possess information about regions in order-parameter space where the solid is unstable and where the Hessian of the free energy has negative eigenvalues. These regions can be accessed using umbrella sampling[48] to estimate the unstable part of the free energy[49–51]. In the context of alloys, bias potentials are typically added to *composition* variables to estimate the free energy within the spinodal of a miscibility gap. Here we extend this approach to probe the free energy surface as a function of order parameters where free energy curvatures may be negative. This can be achieved by adding bias potentials that are functions of the order parameters according to:

$$\Theta = \sum_{\vec{\sigma}} \exp\left(-\frac{E(\vec{\sigma}) + M\sum_i \phi_i(\eta_i(\vec{\sigma})-\kappa_i)^2}{k_B T}\right) \tag{32}$$

where the bias potential is centered about κ_i and has a curvature that is related to ϕ_i. In this ensemble, we are free to choose the values of κ_i and ϕ_i. Metropolis Monte Carlo can then be used to calculate ensemble averages of the order parameters, η_i, and other extensive quantities such as the average energy, $\bar{E}$ etc. Similar to other umbrella sampling schemes[49–51], the partition function in eq. (32) can alternatively be written as:

$$\begin{aligned}\Theta &= \sum_{\vec{\eta}} \exp\left(-\frac{M\sum_i \phi_i(\eta_i-\kappa_i)^2}{k_B T}\right)\sum_{\vec{\sigma}} \exp\left(-\frac{E(\vec{\sigma})}{k_B T}\right)\delta\left(\vec{\eta}(\vec{\sigma})-\vec{\eta}\right)\\ &= \sum_{\vec{\eta}} \exp\left(-\frac{G(\vec{\eta},T) + M\sum_i \phi_i(\eta_i-\kappa_i)^2}{k_B T}\right)\end{aligned}$$

Here, the outer sum is over all possible values of $\vec{\eta}$ corresponding to configurations that are accesible in the real system and $G(\vec{\eta},T)$ is the coarse-grained free energy of eq. (30) evaluated for order parameters $\vec{\eta}$ and temperature T.

In the thermodynamic limit, the probability distribution of states having a particular value of the order parameters $\vec{\eta}$ is expected to be peaked at their average values, $\langle\vec{\eta}\rangle$, such that the derivative of Θ with respect to any order parameter, η_i, should be zero when evaluated at the equilibrium values of the order parameters:

$$\left.\frac{\partial\Theta}{\partial\eta_i}\right|_{\langle\vec{\eta}\rangle} = 0 \approx \left.\frac{\partial \exp\left(-\frac{G(\vec{\eta},T)+M\sum_i \phi_i(\eta_i-\kappa_i)^2}{k_B T}\right)}{\partial\eta_i}\right|_{\langle\vec{\eta}\rangle} \tag{33}$$

Simplifying this equation, yields:

$$\frac{1}{M}\frac{\partial G}{\partial \eta_i}\bigg|_{\langle\vec{\eta}\rangle} = -2\phi_i(\langle\eta_i\rangle - \kappa_i) \tag{34}$$

This last equation is the key to calculating free energies as a function of order parameters. Semi-grand canonical Monte Carlo simulations can be used to calculate ensemble averages of the order parameters $\langle\vec{\eta}\rangle$ as a function of ϕ_i, κ_i and T. By mapping out a path in ϕ_i and κ_i space that connects to a reference state where the free energy is known, it becomes possible to integrate eq. (34) to calculate the free energy at an arbitrary value of $\vec{\eta}$.

IV. CASE STUDIES

We illustrate the calculation of free energies as a function of order parameters and temperature for two examples. The first focuses on an order-disorder transition predicted by the well studied Ising Hamiltonian for a triangular lattice having nearest neighbor (NN) and next nearest neighbor (NNN) pair interactions[52]. In the second example we explore the free energy surface as a function of order parameters that link the Ni-rich fcc solid solution to the $L1_2(Ni_3Al)$ ordering within the Ni-Al binary.

A. Triangular lattice and the row ordering

The Ising model with nearest neighbor ($J_{\rm NN}$) and next-nearest neighbor interactions ($J_{\rm NNN}$) predicts a rich variety of low-temperature orderings when the ratio of interactions ($\frac{J_{\rm NN}}{J_{\rm NNN}}$) is 10 (using spin based occupation variables, i.e. $\sigma_i = \pm 1$)[53]. Of particular interest is the row ordering shown in Figure 7 at a composition of 0.5. It undergoes a first order phase transition to the disordered phase upon heating[52]. The formation of row-orderings on a triangular lattice are found in many technological applications such as the adsorption of gases on metal surfaces[10,11] and the intercalation of lithium into cathode materials[54,55].

As described in Section II B, suitable order parameters for the row ordering can be expressed as linear combinations of the sublattice compositions within a (2×2) supercell (fig. 8) of the primitive cell using the transformation matrix of eq. (15). The first order parameter η_0 corresponds to the global composition, while the other order parameters describe the extent of long-range order similar to the row ordering. Figure 9 shows the locations of the six symmetrically equivalent variants of the row orderings in η_1, η_2 and η_3 space. The origin in this space corresponds to the disordered phase. Of interest is the dependence of the free energy landscape on temperature and order parameters.

Figure 10 shows a portion of the phase diagram around $x = 0.5$ as calculated with Monte Carlo simulations applied to the Ising Hamiltonian. The row ordering undergoes a first-order phase transition to the disordered phase at elevated temperatures. Figure 10 also shows free energies calculated by integrating eq. (34) using data collected with Monte Carlo simulations in a biased ensemble (eq. (32)). The free energies are plotted along the η_1 order parameter axis that connects two translational variants (i.e. the line corresponding to $\eta_2 = \eta_3 = 0$ in fig. 9). The translational variants that lie along this line consist of rows that are oriented along the same direction but are translated by a primitive lattice translation relative to each other. The disordered phase corresponds to a value of zero along this axis.

At elevated temperatures, Figure 10 shows that the free energy as a function of order parameter is convex, with the lowest free energy corresponding to the disordered phase ($\eta = 0$). At this temperature, the ordered phases have a higher free energy than the disordered phase. Furthermore, they are also unstable as there are no local minima at finite values of the order parameters (Figure 10). As the temperature is lowered to values closer to the order/disorder temperature, but still above it, the free energy landscape qualitatively changes. The disordered phase continues to have the lowest free energy, but the ordered phases become locally stable. The row orderings and the disordered phase are separated from each other by a small free energy barrier. At this temperature, the ordered phase is metastable while the disordered phase is still globally stable. Figure 10 shows that a further reduction of the temperature to below the order/disorder temperature reverses the relative stability between the ordered and disordered phases. The row ordering now has the lowest free energy, but the disordered solid solution still remains metastable residing in a free energy well. Lowering the temperature even further, makes the disordered phase unstable. Anti-phase boundaries separating two translational variants form within the Monte Carlo simulations cells. This leads to the flat portion of the free energy around $\eta_1 \approx 0$ since a variation of the order parameter when anti-phase boundaries are present only changes the relative fraction of one translational variant relative to the other. The anti-phase boundary free energy may be extracted from this free energy landscape in a manner similar to that described by Sadigh and Erhart[49] for interfacial free energies between coexisting phases within a miscibility gap.

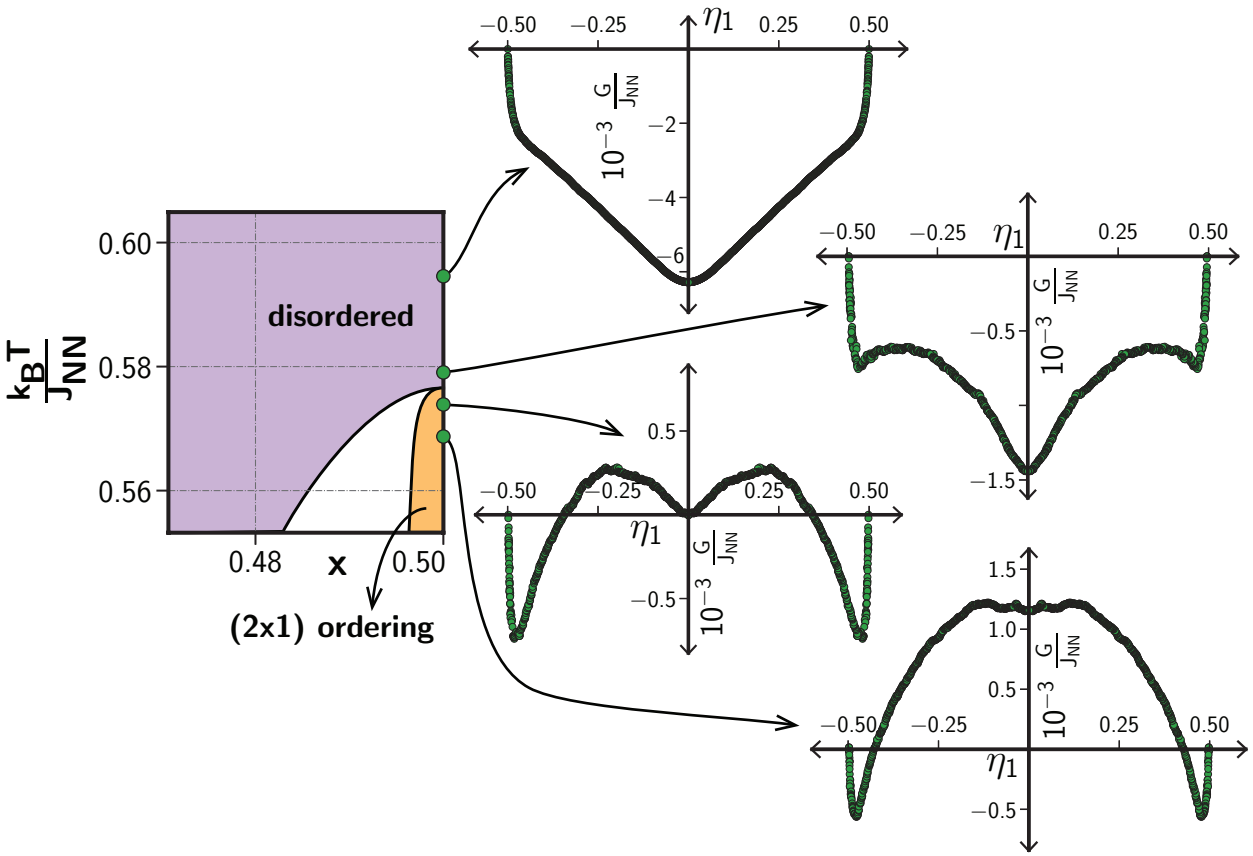

FIG. 10. Phase diagram and free energies for a model Hamiltonian on the triangular lattice with $\frac{J_{NN}}{J_{NNN}} = 10$. The temperature and free energies are scaled based on the nearest neighbor interaction. Free energies are mirrored across $\eta_1 = 0$ due to the symmetry of the domain.

The free energy landscapes of Figure 10 provide a means with which to extract not only the thermodynamic order-disorder transformation temperature, but also the temperatures of ordering and disordering spinodals. The ordering spinodal corresponds to the temperature at which the disordered phase becomes unstable. It is the temperature at which the curvature of the free energy at the origin in order parameter space (i.e. for the disordered state) transitions from positive to negative. The ordering spinodal occurs below the order-disorder transition temperature. The disordering spinodal occurs above the thermodynamic transition temperature and corresponds to the temperature where a superheated ordered phase becomes unstable. It is the temperature at which the barrier separating the ordered phase from the disordered phase disappears. The ordering and disordering spinodals signify transitions in the kinetic mechanism with which an order-disorder transition can occur. When a disordered phase is cooled to a temperature below the thermodynamic transition temperature but above the ordering spinodal, it can only transform through a localized nucleation and growth mechanism since the disordered phase is still metastable. However, if the disordered phase is supercooled below the ordering spinodal, it becomes unstable and will begin to order in a continuous manner and uniformly throughout the solid.

B. γ/γ' in Ni-Al alloys

Nickel-based superalloys are widely used as high-temperature materials in the aerospace industry[1]. Commercial alloys used in jet engines employ a two-phase mixture of an ordered $L1_2$ intermetallic (e.g. γ'-Ni_3Al) coherently embedded within a nickel-rich disordered solid solution (γ). Alloy compositions are chosen to optimize the shape, morphology and composition of the $L1_2$ precipitates in order to boost high-temperature strength. A detailed analysis of phase stability starting from first principles in the prototypical Ni-Al binary alloy has been recently described by Goiri and Van der Ven[2]. A portion of the FCC phase diagram as calculated with Monte Carlo simulations applied to a first-principles cluster expansion for FCC Ni-Al is shown in Figure 11. It consists of a two-phase field that separates

the γ FCC solid solution from the $L1_2$ ordered γ' phase.

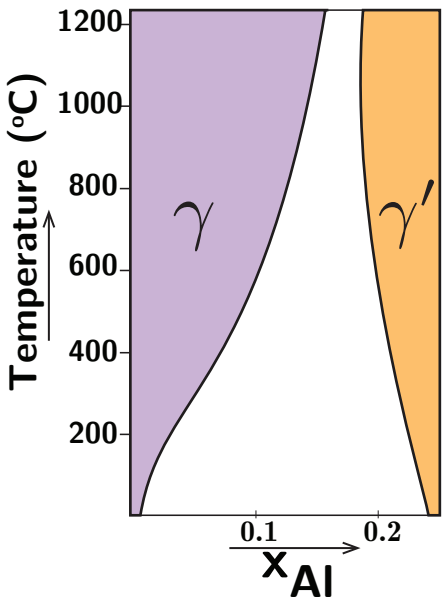

FIG. 11. Ni-rich part of the phase diagram for the Ni-Al binary alloy calculated from Monte Carlo simulations on a cluster expansion Hamiltonian parameterized from first-principles[2]

The symmetry adapted order parameters that describe the symmetry breaking associated with $L1_2$ ordering were described in Section II A and are given by Equations (4) to (7). They are defined as linear combinations of the sublattice compositions in the conventional FCC cell (Figure 4).

Free energies were determined by integrating the chemical potential and average order parameter values as calculated with Monte-Carlo simulations within the biased ensemble (eq. (32)) using the cluster expansion Hamiltonian as parametrized by Goiri *et al.*[2]. The full free energy generated for this system spans 5 dimensions at constant temperature (4 order parameters and the the free energy). To visualize this multi-dimensional free energy landscape, we project it onto a two-dimensional subspace in Figure 12a. The two-dimensional subspace is spanned by the average composition of the alloy, x_{Al}, and a high symmetry path in η_1, η_2 and η_3 space, parametrically represented by ξ defined as

$$\xi = \frac{\eta_1 + \eta_2 + \eta_3}{\sqrt{3}} \tag{35}$$

This path follows the dashed line connecting the origin to one of the corners of the tetrahedron in Figure 6 corresponding to a particular translational variant of $L1_2$.

Figure 12a shows the calculated free energy as a function of x_{Al} and the projected order parameter, ξ, at 600 K. The size of the tetrahedron of allowed values for η_1, η_2 and η_3 in fig. 6 depends on concentration and shrinks as the concentration is reduced below $x_{\mathrm{Al}} = 0.25$. The maximum allowed value of ξ, which measures the distance from the origin to one of the corners of the tetrahedron in order parameter space (fig. 6), therefore, decreases linearly to zero as the concentration of the alloy is decreased to zero. As a result, the allowed values of concentration x_{Al} and projected order parameter ξ fall in a triangle in fig. 12a. The free energy is referenced to the free energy of pure Ni and perfectly ordered $L1_2$ at 0K.

At low Al concentrations, the minimum of the free energy occurs along the $\xi = 0$ line. The Ni-rich alloy therefore does not exhibit any long-range order and forms a disordered solid solution. At higher aluminum compositions, there is second minimum in the free energy albeit at a non-zero value of the order parameter, corresponding to $L1_2$ ordering. It is instructive to consider the path of the order parameters that minimizes the free energy at fixed x_{Al} in fig. 12a:

$$\vec{\eta}(x_{\mathrm{Al}}, T) = \underset{\vec{\eta}}{\operatorname{argmin}}\ G(x_{\mathrm{Al}}, \vec{\eta}, T) \tag{36}$$

The path in x_{Al}-ξ space is shown by a dashed line in fig. 12a. At low concentrations, the value of ξ minimizing the free energy is zero, but abruptly increases inside the two phase region, reaching its maximum value as x_{Al} approaches 0.25, the composition of perfectly ordered $L1_2$. Figure 12b shows the free energy along this path as a function of

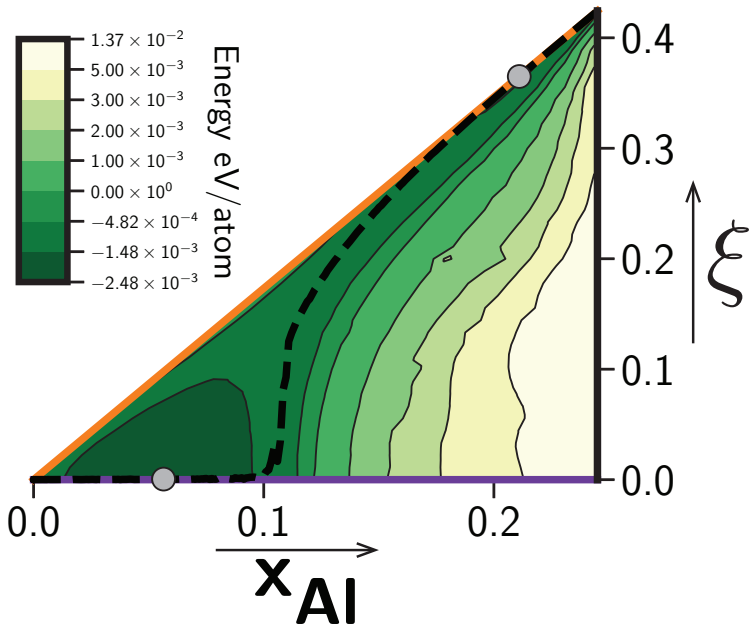

(a) Free energy as a function of aluminum composition and the lower dimensional order parameter(ξ) calculated from Monte Carlo at 600K. The minimum free energy path of eq. (36) is outlined as a black dashed line. The points on the common tangent across composition are shown in grey. The extreme sections corresponding to the disordered (purple) and the ordered (orange) phases are also highlighted.

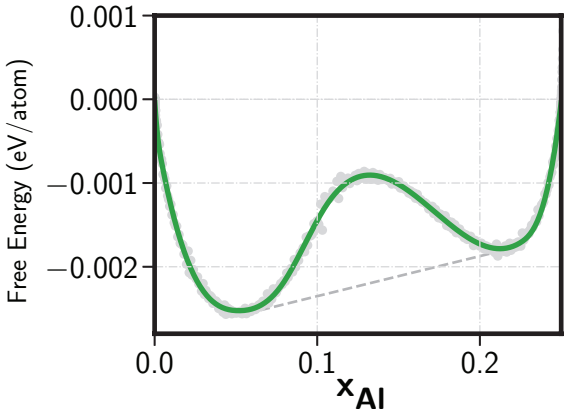

(b) Free energy as a function of composition, minimized along the order parameter as defined by eq. (36). The integrated data from Monte Carlo calculations is shown in light grey, with the green spline drawn on top as a guide to the eye. The common tangent is shown as the dashed grey line.

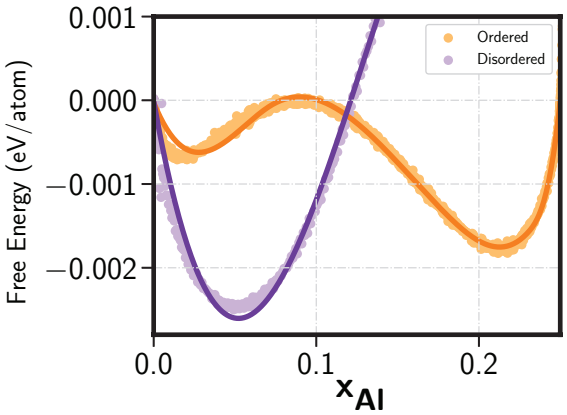

(c) Sections of the free energy surface for a disordered (purple) and ordered (orange) phase. The integrated free energies from Monte Carlo are shown as the lighter colored points, with the spline fits drawn as a guide to the eye.

FIG. 12. Free energy surfaces and sections calculated from biased Monte-Carlo sampling on a cluster expansion Hamiltonian parameterized from first-principles calculations. The ensemble averages were calculated at 600K.

composition. This is the free energy for a homogeneous Ni-Al alloy in which the Ni and Al have achieved their equilibrium degree of long-range order. Application of the common tangent construction to this free energy curve determines the bounds of the two-phase region separating the Ni-rich solid solution from $L1_2$ ordering.

It is also instructive to consider the free energy along other paths in x_{Al}-ξ space. The free energy of the disordered phase corresponds to the locus of points along the composition axis having $\xi = 0$. This free energy is shown as the purple curve in fig. 12c. The orange curve in fig. 12c corresponds to the free energy as a function of composition when the solid has the maximum degree of $L1_2$ type ordering. This curve exhibits two wells, but the well at low

concentrations is well above that of the disordered phase.

While free energy surfaces such as those of fig. 12 are necessary to establish the equilibrium state, they also have relevance in determining the kinetic pathways that an ordering transformation may follow. A common practice is to quench a disordered solid solution such as γ into a two-phase field to precipitate a dispersion of an ordered phase. The mechanism with which an ordering transformation occurs will depend on whether the Hessian of the free energy of the quenched solid has only positive eigenvalues or whether it has at least one negative eigenvalue (unstable). If all eigenvalues are positive, the quenched phase is locally stable and the ordering reaction will occur with a nucleation and growth mechanism. If the quenched in phase is unstable, the transformation will proceed continuously. It is possible to distinguish two time scales during a continuous ordering reaction. The first is a rapid relaxation involving a relatively small number of atomic hops that are required to reorder the atoms. While the local concentration does not change much on this time scale, the local value of the order parameters may evolve rapidly until the minimum in the free energy has been reached at fixed local concentration. The second, longer time-scale process, involves long-range diffusion that is required to redistribute atoms to form a two-phase mixture consisting of phases with very different compositions. If the two time scales are very different, they can be decoupled. The phase separation process will then proceed similar to a spinodal decomposition reaction following a path in order parameter space coinciding with the minimum free energy. Since the order parameter locally adopts its equilibrium value that depends on the local concentration, the kinetics can be described with a Cahn-Hilliard approach relying on free energy that only depends on concentration. For the Ni-Al alloy this would be the free energy curve of fig. 12b. If the two processes cannot be decoupled, then the full free energy surface as a function of both concentration and order parameters must be considered. The kinetics of this decomposition would need to be described with a coupled Cahn-Hilliard and Allen-Cahn approach.

V. DISCUSSION AND CONCLUSION

We have introduced a general approach to generate symmetry adapted order parameters for any order-disorder transformation in a crystalline solid. The order parameters are expressed as linear combinations of sublattice compositions in a reference supercell that can accommodate all the symmetrically equivalent variants of a particular ordering. The algorithm constructs the order parameters to be adapted to the high symmetry of the disordered phase, thereby making it possible to distinguish between the disordered phase and all symmetrically equivalent variants of the ordered phase with a minimal set of descriptors. While we have introduced the approach for binary alloys, it can easily be extended to multicomponent alloys having more than two elements. An additional composition variable for each additional alloying element must then be assigned to each sublattice site of the mutually commensurate supercell. All subsequent steps are identical to that described here for a binary alloy. We have also introduced a thermodynamic formalism to enable the calculation of free energies as a function of symmetry adapted order parameters. A key element of this formalism is the definition of sublattice chemical potentials that are conjugate to sublattice concentrations. The use of sublattice chemical potentials, together with umbrella sampling and free energy integration techniques, makes it possible to explore metastable and unstable portions of the free energy surface in Monte Carlo simulations.

Free energy surfaces as a function of order parameters can provide rich insights, not only about the equilibrium properties of multi-component solids that exhibit ordered phases, but also about the kinetic mechanisms of order-disorder transitions. Soffa and Laughlin developed a "graphical thermodynamic approach" that relies on free energy surfaces similar to those of fig. 12 to identify and rationalize ordering reactions in different alloys. The approach developed here now makes it possible to calculate such free energy surfaces from first principles for technologically important solids.

The coarse-graining scheme to calculate free energies relies on two ingredients: a method to calculate the energy of the crystal for arbitrary orderings and a method to estimate the free energy from Monte Carlo simulations. In this study we used a cluster expansion Hamiltonian to describe interatomic interactions. Alternate interatomic potentials such as the semi-empirical embedded atom method (EAM)[56,57], ReaxFF[58] or an artificial neural network potential parameterized from first principles[59] can also be used, provided they accurately describe the relative energies between different atomic configurations on a parent crystal structure. To calculate free energies, we used umbrella sampling coupled with free energy integration techniques. There are alternate approaches to directly estimate the free energy including histogram sampling methods such as Wang-Landau[60] or metadynamics[61] that are capable of probing high-dimensional energy landscapes accurately.

The methodological developments of this work brings us a step closer to enabling a truly first-principles treatment of kinetic processes associated with order-disorder phase transformations in the solid state. Phenomenological phase-field methods based on the Cahn-Hilliard and Allen-Cahn theories of continuous phase transformations are capable of describing the kinetic evolution of phase decomposition and ordering reactions at the meso and macroscopic scales. They depend on thermodynamic and kinetic functions that are determined by the chemistry and crystal structure

of the phases participating in the phase transformation. The ability to identify suitable order parameters and to calculate free energies as a function of those order parameters, along with methods to calculate kinetic transport coefficients[36], is crucial to establishing a rigorous link between electronic structure calculations and phenomenological theories of non-equilibrium processes.

VI. ACKNOWLEDGEMENTS

We are grateful for financial support from the U.S. Department of Energy, Office of Basic Energy Sciences, Division of Materials Sciences and Engineering under Award #DE-SC0008637 as part of the Center for PRedictive Integrated Structural Materials Science (PRISMS Center) at University of Michigan. Additional support from the Office of Naval Research under Grant No. N00014-12- 1-0013 is acknowledged. Computing resources were also provided by the Center for Scientific Computing at the CNSI and MRL under NSF MRSEC(DMR-1121053) and NSF CNS-0960316. All graphs were made with the `matplotlib`[62] library.

Appendix A: Obtaining mutually commensurate supercells

We wish to find a solution to the mutually commensurate supercell relation

$$\mathcal{S} = \boldsymbol{P}\mathcal{T} = (\boldsymbol{P}\boldsymbol{T}^{(i)})\boldsymbol{V}^{(i)}, \forall \boldsymbol{T}^{(i)} \in \mathbb{T}, \tag{A1}$$

which states that there is a supercell $\mathcal{S}$ that is related to the primitive cell lattice vectors $\boldsymbol{P}$ via the full-rank integer matrix $\mathcal{T}$ and can also be written as a supercell of two or more smaller supercells of $\boldsymbol{P}$. These smaller supercells that tile, or are *commensurate*, with $\mathcal{S}$ are given by $\boldsymbol{S}^{(i)} = \boldsymbol{P}\boldsymbol{T}^{(i)}$, and the various $\{\boldsymbol{T}^{(i)}\}$ are specified by the set $\mathbb{T}$. Each smaller supercell is related to $\mathcal{S}$ via $\mathcal{S} = \boldsymbol{S}^{(i)}\boldsymbol{V}^{(i)}$, where $\boldsymbol{V}^{(i)}$ is also a full-rank integer matrix.

We first consider the case of finding the mutually commensurate supercell of two smaller supercells $\boldsymbol{S}^{(1)}$ and $\boldsymbol{S}^{(2)}$ having integer transformation matrices $\boldsymbol{T}^{(1)}$ and $\boldsymbol{T}^{(2)}$. We additionally impose the restriction that $\det(\mathcal{S})$ be minimized (i.e., we are attempting to find the smallest possible mutually commensurate supercell. Stated mathematically, we wish to solve

$$\boldsymbol{P}\boldsymbol{T}^{(1)}\boldsymbol{V}^{(1)} = \boldsymbol{P}\boldsymbol{T}^{(2)}\boldsymbol{V}^{(2)} \tag{A2}$$

for integer matrices $\boldsymbol{V}^{(1)}$ and $\boldsymbol{V}^{(2)}$, where $|\det(\boldsymbol{V}^{(1)})|$ is minimized. After multiplying through by $\boldsymbol{P}^{-1}$, Equation (A2) reduces to

$$\boldsymbol{T}^{(1)}\boldsymbol{V}^{(1)} = \boldsymbol{T}^{(2)}\boldsymbol{V}^{(2)}. \tag{A3}$$

If we define the matrix $\boldsymbol{M} = \det(\boldsymbol{T}^{(1)})\boldsymbol{T}^{(1)-1}\boldsymbol{T}^{(2)}$, then $\boldsymbol{M}$ is an integer matrix and we can rewrite eq. (A3) as

$$\boldsymbol{V}^{(1)} = \frac{\boldsymbol{M}\boldsymbol{V}^{(2)}}{\det(\boldsymbol{T}^{(1)})}, \tag{A4}$$

and we must find an integer matrix $\boldsymbol{V}^{(2)}$ such that $\boldsymbol{V}^{(1)}$ is integer and $\det(\boldsymbol{V}^{(2)})$ is minimized. We can define the Smith normal form of $\boldsymbol{M}$ as $\boldsymbol{M} = \boldsymbol{U}\boldsymbol{D}\boldsymbol{W}$, where $\boldsymbol{U}$ and $\boldsymbol{W}$ are integer unimodular matrices, and $\boldsymbol{D}$ is an integer diagonal matrix. Additionally, diagonal elements of $\boldsymbol{D}$ satisfy $D_{i,i}|D_{i+1,i+1}$ (i.e., the element $D_{i,i}$ is divisible by $D_{i+1,i+1}$). Inserting the Smith normal form into eq. (A4) yields

$$\boldsymbol{V}^{(1)} = \frac{\boldsymbol{U}\boldsymbol{D}\boldsymbol{W}\boldsymbol{V}^{(2)}}{\det(\boldsymbol{T}^{(1)})}. \tag{A5}$$

Equation (A5) is satisfied when $\boldsymbol{V}^{(2)} = \boldsymbol{W}^{-1}\boldsymbol{Z}$, where $\boldsymbol{Z}$ is a diagonal matrix. Each element $Z_{i,i}$ must be the smallest integer such that $D_{i,i}Z_{i,i}$ is divisible by $\det(\boldsymbol{T}^{(1)})$. This condition is satisfied when $Z_{i,i} = \det(\boldsymbol{T}^{(1)})/\gcd(D_{i,i}, \det(\boldsymbol{T}^{(1)}))$. Thus, the final solution is

$$\boldsymbol{V}^{(1)} = \boldsymbol{U}\boldsymbol{D}\boldsymbol{Z} \tag{A6}$$

$$\boldsymbol{V}^{(2)} = \boldsymbol{W}^{-1}\boldsymbol{Z}. \tag{A7}$$

The use of the Smith normal form, which provides a unique set of elementary divisors via the matrix $\boldsymbol{D}$, removes any ambiguity in the relative definition of $\boldsymbol{T}^{(1)}$ and $\boldsymbol{T}^{(2)}$, such that $\boldsymbol{V}^{(1)}$ and $\boldsymbol{V}^{(2)}$ are unique to within simultaneous

multiplication by a unimodular integer matrix. As such, the solution can be performed iteratively, so that to find the mutually commensurate supercell among three supercells $\{\boldsymbol{T}^{(1)}, \boldsymbol{T}^{(2)}, \boldsymbol{T}^{(3)}\}$, we can first find the mutually commensurate supercell $\boldsymbol{T}^{(1,2)}$ of $\boldsymbol{T}^{(1)}$ with $\boldsymbol{T}^{(2)}$ and then find the mutually commensurate supercell $\boldsymbol{T}^{(1,2,3)}$ of $\boldsymbol{T}^{(1,2)}$ with $\boldsymbol{T}^{(3)}$.

---

* avdv@engineering.ucsb.edu

[1] T. M. Pollock and S. Tin, Journal of Propulsion and Power **22**, 361 (2006).
[2] J. G. Goiri and A. Van der Ven, Physical Review B **94** (2016), 10.1103/PhysRevB.94.094111.
[3] J.-F. Nie, Metallurgical and Materials Transactions A **43**, 3891 (2012).
[4] A. R. Natarajan, E. L. S. Solomon, B. Puchala, E. A. Marquis, and A. Van der Ven, Acta Materialia **108**, 367 (2016).
[5] A. R. Natarajan and A. Van der Ven, Physical Review B **95**, 214107 (2017).
[6] A. R. Natarajan and A. Van der Ven, Acta Materialia **124**, 620 (2017).
[7] J. Androulakis, C. H. Lin, H. J. Kong, C. Uher, C. I. Wu, T. Hogan, B. A. Cook, T. Caillat, K. M. Paraskevopoulos, and M. G. Kanatzidis, Journal of the American Chemical Society **129**, 9780 (2007).
[8] J. W. Doak and C. Wolverton, Physical Review B **86** (2012), 10.1103/PhysRevB.86.144202.
[9] K. Biswas, J. He, I. D. Blum, C.-I. Wu, T. P. Hogan, D. N. Seidman, V. P. Dravid, and M. G. Kanatzidis, Nature **489**, 414 (2012).
[10] B. C. Han, A. Van der Ven, G. Ceder, and B. J. Hwang, Physical Review B **72**, 1 (2005).
[11] H. Tang, A. Van Der Ven, and B. L. Trout, Physical Review B **70**, 1 (2004).
[12] L. Cao and T. Mueller, The Journal of Physical Chemistry C **119**, 17735 (2015).
[13] L. Cao and T. Mueller, Nano Letters **16**, 7748 (2016).
[14] X. Huang, Z. Zhao, L. Cao, Y. Chen, E. Zhu, Z. Lin, M. Li, A. Yan, A. Zettl, Y. M. Wang, X. Duan, T. Mueller, and Y. Huang, Science **348**, 1230 (2015).
[15] A. Van der Ven, G. Ceder, M. Asta, and P. D. Tepesch, Physical Review B **64** (2001), 10.1103/PhysRevB.64.184307.
[16] J. Briant and G. Farrington, Journal of Solid State Chemistry **33**, 385 (1980).
[17] J. P. Boilot, G. Collin, P. Colomban, and R. Comes, Physical Review B **22**, 5912 (1980).
[18] M. D. Radin, S. Hy, M. Sina, C. Fang, H. Liu, J. Vinckeviciute, M. Zhang, M. S. Whittingham, Y. S. Meng, and A. Van der Ven, Advanced Energy Materials , 1602888 (2017).
[19] J. W. Cahn and J. E. Hilliard, The Journal of Chemical Physics **28**, 258 (1958).
[20] S. Allen and J. Cahn, Acta Metallurgica **27**, 1085 (1979).
[21] L.-Q. Chen, Annual Review of Materials Research **32**, 113 (2002).
[22] V. Vaithyanathan, C. Wolverton, and L. Chen, Physical Review Letters **88**, 125503 (2002).
[23] L.-Q. Chen and Y. Wang, JOM **48**, 13 (1996).
[24] N. Moelans, B. Blanpain, and P. Wollants, Calphad **32**, 268 (2008).
[25] J. Sanchez, F. Ducastelle, and D. Gratias, Physica A: Statistical Mechanics and its Applications **128**, 334 (1984).
[26] D. de Fontaine, Solid state physics **47**, 33 (1994).
[27] M. Asta, C. Wolverton, D. De Fontaine, and H. Dreyssé, Physical Review B **44**, 4907 (1991).
[28] P. E. A. Turchi and A. Gonis, eds., *Statics and Dynamics of Alloy Phase Transformations*, NATO ASI Series, Vol. 319 (Springer US, Boston, MA, 1994).
[29] D. P. Laks and L. Ferreira, Physical Review B **46**, 12587 (1992).
[30] G. Ceder, Computational Materials Science **1**, 144 (1993).
[31] F. Zhou, T. Maxisch, and G. Ceder, Physical Review Letters **97** (2006), 10.1103/PhysRevLett.97.155704.
[32] A. van de Walle and G. Ceder, Journal of Phase Equilibria **23**, 348 (2002).
[33] W. Zhong, D. Vanderbilt, and K. M. Rabe, Physical Review Letters **73**, 1861 (1994).
[34] W. Zhong, D. Vanderbilt, and K. M. Rabe, Physical Review B **52**, 6301 (1995).
[35] A. van de Walle and M. Asta, Modelling and Simulation in Materials Science and Engineering **10**, 521 (2002).
[36] A. Van der Ven, H. C. Yu, G. Ceder, and K. Thornton, Progress in Materials Science **55**, 61 (2010).
[37] L. J. Nelson, G. L. W. Hart, F. Zhou, and V. Ozoliņš, Physical Review B **87** (2013), 10.1103/PhysRevB.87.035125.
[38] L. J. Nelson, V. Ozoliņš, C. S. Reese, F. Zhou, and G. L. W. Hart, Physical Review B **88** (2013), 10.1103/PhysRevB.88.155105.
[39] J. C. Thomas and A. Van der Ven, Physical Review B **88**, 214111 (2013).
[40] J. C. Thomas and A. Van der Ven, Physical Review B **90** (2014), 10.1103/PhysRevB.90.224105.
[41] R. J. Braun, J. W. Cahn, G. B. McFadden, and A. A. Wheeler, Philosophical Transactions of the Royal Society of London A: Mathematical, Physical and Engineering Sciences **355**, 1787 (1997).
[42] J. C. Thomas and A. Van der Ven, Journal of the Mechanics and Physics of Solids (2017), 10.1016/j.jmps.2017.06.009.
[43] G. L. W. Hart and R. W. Forcade, Physical Review B **77** (2008), 10.1103/PhysRevB.77.224115.
[44] CASM Developers, "CASM: A Clusters Approach to Statistical Mechanics," (2016).
[45] M. Kardar, *Statistical Physics of Fields*, 1st ed. (Cambridge University Press, 2007).
[46] Q. Xu and A. Van der Ven, Intermetallics **17**, 319 (2009).
[47] A. S. Dalton, A. A. Belak, and A. Van der Ven, Chemistry of Materials **24**, 1568 (2012).

[48] G. M. Torrie and J. P. Valleau, Journal of Computational Physics **23**, 187 (1977).
[49] B. Sadigh and P. Erhart, Physical Review B **86**, 134204 (2012).
[50] Y. Mishin, Modelling and Simulation in Materials Science and Engineering **22**, 045001 (2014).
[51] B. Sadigh, P. Erhart, A. Stukowski, A. Caro, E. Martinez, and L. Zepeda-Ruiz, Physical Review B **85** (2012), 10.1103/PhysRevB.85.184203.
[52] J. Glosli and M. Plischke, Canadian journal of physics **61**, 1515 (1983).
[53] F. Ducastelle, *Order and Phase Stability in Alloys*, Cohesion and structure (Elsevier, 1991).
[54] A. Van der Ven, M. K. Aydinol, and G. Ceder, Journal of The Electrochemical Society **145**, 2149 (1998).
[55] C. Wolverton and A. Zunger, Physical review letters **81**, 606 (1998).
[56] M. S. Daw and M. I. Baskes, Physical review letters **50**, 1285 (1983).
[57] M. S. Daw, S. M. Foiles, and M. I. Baskes, Materials Science Reports **9**, 251 (1993).
[58] A. C. T. van Duin, S. Dasgupta, F. Lorant, and W. A. Goddard, The Journal of Physical Chemistry A **105**, 9396 (2001).
[59] J. Behler and M. Parrinello, Physical Review Letters **98** (2007), 10.1103/PhysRevLett.98.146401.
[60] F. Wang and D. P. Landau, Physical Review Letters **86**, 2050 (2001).
[61] A. Barducci, M. Bonomi, and M. Parrinello, Wiley Interdisciplinary Reviews: Computational Molecular Science **1**, 826 (2011).
[62] J. D. Hunter, Computing In Science & Engineering **9**, 90 (2007).